



Soft Matter

Soft actuators by electrochemical oxidation of liquid metal surfaces

Journal:	<i>Soft Matter</i>
Manuscript ID	SM-ART-10-2020-001851.R1
Article Type:	Paper
Date Submitted by the Author:	26-Nov-2020
Complete List of Authors:	Liao, Jiahe; Carnegie Mellon University, Robotics Majidi, Carmel; Carnegie Mellon University, Mechanical Engineering

SCHOLARONE™
Manuscripts

Cite this: DOI: 00.0000/xxxxxxxxxx

Soft actuators by electrochemical oxidation of liquid metal surfaces

Jiahe Liao^{*a} and Carmel Majidi^a

Received Date

Accepted Date

DOI: 00.0000/xxxxxxxxxx

The surface energy of liquid metals can be electrochemically controlled over a wide range of values – from near zero to 500 mJ/m² – using low voltage potential. ($\sim 1V$). This enables the ability to create soft-matter actuators that exhibit high work density at small scales. We demonstrate that a liquid metal (LM) meniscus wetted between two copper pads can function as an electrochemical soft actuator whose force and shape are controllable by tuning LM surface energy. Energy minimization models are presented in order to predict actuator performance as a function of the LM droplet and Cu pad dimensions. The results suggest that the electrochemical LM actuator has a unique combination of high work density, biologically-relevant activation frequency, and low operational voltage that stands out from other classes of soft-matter actuators.

1 Introduction

Soft robotic systems typically operate through the use of soft actuators constructed from highly deformable materials or liquids. Because of their intrinsic compliance, these actuators can achieve elastic resilience and adaptability similar to their biological counterparts^{1–4}. One challenge with engineering these artificial muscles is the selection of soft materials and activation methods while maintaining desired static and dynamic performance. Every actuator, by their operating principles, can have high performance by some metrics and low performance by other metrics. Dielectric elastomer actuators (DEA), for example, have excellent work density (10–150kJ/m³^{5,6}) but requires high voltages ($\sim 1kV$) due to the Maxwell stress requirement. In many robotic applications such as surgical and underwater robots, this may be an unsafe choice of actuator. Shape memory alloy (SMA), another actuator known for high work density ($\sim 1MJ/m^3$ ^{1,7}), suffers from low efficiency and may not be satisfactory for every robotic design.

Liquid metals provide great opportunities for creating an artificial muscle that generates forces with scaling advantage due to dominating surface tension at small length scales (L), has high work density with smaller L , and does not have voltage or efficiency issues like DEA and SMA. Eutectic gallium-indium (EGaIn) has been shown to have electrochemically controllable surface tension (between ~ 500 mN/m to near zero) when submerged in NaOH solution with ~ 1 V pulses^{8–10}. The rapid and reversible oxidation of the gallium surface creates a surfactant-like oxide layer that disrupts the surface energy and hence changes the equilibrium shape. The same phenomenon was demonstrated in electric field-driven manipulation^{11–13,13–20} and actuation^{21–25} of EGaIn droplets. In all cases, the change in electric potential causes a re-

dox reaction, which leads to the deposition or removal of gallium oxide and hence the change in surface energy.

Here, we introduce a muscle-inspired soft actuator that is composed of an axis-symmetric capillary bridge of EGaIn, which linearly contracts or expands in response to electrical stimuli. The EGaIn droplet with constant volume V is bridged and alloyed between two identical and parallel copper plates with constant radius R_0 (Fig 1). Because the strength of metallic bonding is dominant at the interface between EGaIn and copper²⁶, the wetting area is assumed to stay constant, preventing the top ring of the EGaIn surface from expanding or receding during actuation. We also require R_0 to be less than the capillary length $R_c = \sqrt{\gamma/(\Delta\rho g)} = 3.2$ mm for reduced EGaIn in order to assume the gravity effect can be ignored compared to surface tension. Because the shape of any liquid can be characterized by the Young-Laplace equation $\Delta P = 2\gamma H$ at any point on the surface²⁷, where ΔP is the pressure drop across the interface, γ is the surface tension, H is the mean curvature, the shape must change in response to the change in γ . However, since the Young-Laplace equation does not have a closed-form solution for most cases²⁷, additional models have to be formalized and numerically solved for the shape.

All types of artificial muscles require a significant change in one or more forms of energy in order to deform or generate forces. This often has strong implications in the static and dynamic performances of an actuator and their scaling laws. For example, for a magnetically-driven actuator with characteristic length L , the magnetic force scales with L^3 ¹. For an electrostatic actuator, the force scales with L^2 ¹. One significant limitation of these actuators is their degraded performance when scale down. By contrast, forces due to surface energies for small fluid bodies, which scale macroscopically with L , strongly suggest that a surface tension-based actuator will have a great scaling advantage at small scales

^a The Robotics Institute, Carnegie Mellon University, 5000 Forbes Ave, Pittsburgh, PA, 15213, USA. E-mail: cmajidi@andrew.cmu.edu.

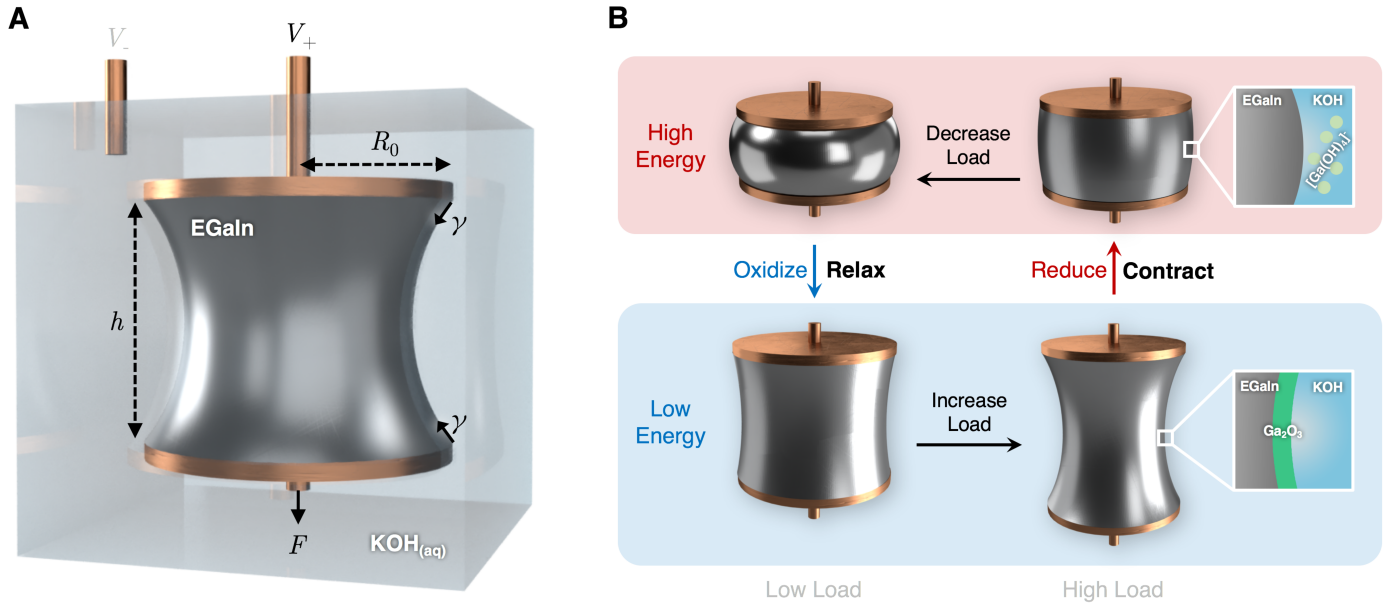


Fig. 1 Overview of the liquid metal actuator. (A) A liquid metal artificial muscle cell is constructed by bridging two identical circular copper plates (radius R_0) with an EGaIn droplet (volume V). The actuator should be operated in an aqueous electrolyte (e.g., KOH) as the medium for electrochemical redox reactions. By varying $V_+ - V_-$, the interfacial tension between the EGaIn and the surrounding KOH can be effectively controlled such that, at the new equilibrium, the muscle length h will be changed. By this principle, the liquid metal actuator operates as an electrochemical artificial muscle with controllable contraction and relaxation. (B) The behavior of the liquid metal actuator is determined by the interfacial reaction between EGaIn and KOH. When the EGaIn droplet is surrounded by KOH electrolyte, Ga at the interface reacts and forms gallate ions $[\text{Ga}(\text{OH})_4]^-$. Relaxation occurs when $V_+ - V_- > \sim 1\text{V}$, which causes $[\text{Ga}(\text{OH})_4]^-$ to react with H^+ from water electrolysis to produce gallium hydroxides $\text{Ga}(\text{OH})_3$, which in turn produces gallium oxides Ga_2O_3 . The gallium oxide layer acts as a surfactant at the EGaIn-KOH interface and drastically lowers the surface tension to near zero⁸. Contraction occurs when the voltage polarity is reversed, which reduces the Ga_2O_3 layer and restores the high surface energy of EGaIn.

(e.g., $L \ll L_c$ where L_c is the capillary length of the fluid) when surface-tension forces dominate over other forces such as gravity.

We examine the geometrical and mechanical behavior of the LM actuator unit by modeling the equilibrium shape at any given loading condition. The models are used to predict the static and dynamic performance of the actuator at varying length scale R_0 and volume V . The theory informs the design rules to achieve a specific performance with the liquid metal actuator.

2 Theory

In order to predict the force-length relationship of a liquid metal actuator, the shape of the liquid bridge is parameterized by (h, f) , where h is the distance between the copper plates and f is a continuous function $f(z)$ over $0 \leq z \leq h$ revolving about z -axis with boundaries $f(0) = f(h) = R_0$ (plate radius) and $f(h/2) = R_1$ (neck radius). We will begin with a simplified model by toroidal approximation, where f can be further parameterized by only the principal radii. Then we will give the exact solution by numerically solving for f subject to the known constraints.

To calculate the equilibrium length of an actuator with prescribed (R_0, V) , let γ be the prescribed surface tension of liquid metal, F be the prescribed axial load including the self weight of liquid metal. The free energy function is

$$E(h, f; R_0, V, \gamma, F) = \gamma A(h, f) - Fh, \quad (1)$$

which should be minimized over all possible h and f , and A is the surface area

$$A(h, f) = 2\pi \int_0^h f \sqrt{1 + f'^2} dz. \quad (2)$$

The equilibrium length is given by

$$h^*(R_0, V, \gamma, F) = \underset{h, f}{\operatorname{argmin}} E(h, f; R_0, V, \gamma, F) \quad (3)$$

$$\text{subject to } \begin{cases} R_0 = f(0) = f(h), \\ V = \pi \int_0^h f^2 dz. \end{cases} \quad (4)$$

2.1 Toroidal approximation model

There may be an infinite number of $f(z)$ functions that satisfy Eq. (4), which suggests that additional constraints are necessary. Analysis can be simplified by imposing the kinematic restriction that the principal radii (R_1, R_2) are each constant across the surface. This assumption can also be interpreted by considering a section of a torus (Fig. 2), with the inner part being a concave or a convex bridge^{28–30}.

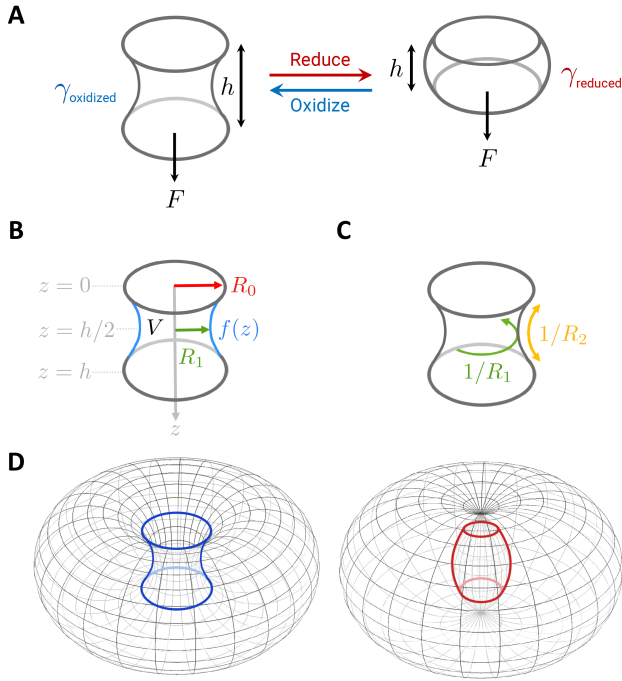


Fig. 2 Models of liquid metal bridges between two solid plates. (A) The equilibrium shape, parameterized by (h, f) , is determined by minimization of free energy $E(h, f) = \gamma A(h, f) - Fh$, where A is the surface area. The surface tension γ is controlled by electrochemical redox reactions, where a higher electric potential causes the oxidation of liquid metal surface and hence a lower surface tension γ_{oxidized} . Likewise, a lower electric potential reduces the liquid metal and drastically increases the surface tension to a higher γ_{reduced} . (B) Assuming axial and longitudinal symmetries, the bridge geometry is characterized by height h and shape profile $f(z)$ over $0 \leq z \leq h$. Exact solutions to $f(z)$ require numerically solving the ODE that arises from the Euler-Lagrange Equation. (C) Toroidal approximation simplifies f to only (h, R_1, R_2) where R_1 and R_2 are the principal radii assumed to be constant across the surface. (D) This assumption can also be interpreted by considering a section of a torus, with the inner part being a concave bridge (left) or a convex bridge (right).

We can now parameterize f by (h, R_1, R_2) as

$$f(z; h, R_1, R_2) = \begin{cases} (R_1 - R_2) - \sqrt{R_2^2 - \left(z - \frac{h}{2}\right)^2} & \text{if } R_1 < R_0 \text{ (concave)} \\ (R_1 - R_2) + \sqrt{R_2^2 - \left(z - \frac{h}{2}\right)^2} & \text{if } R_1 > R_0 \text{ (convex)} \end{cases} \quad (5)$$

In order to reduce the independent variables from (h, R_1, R_2) to only h , we can use Eq. (4) to solve the radius constraint for R_2 and plug it into the volume constraints.

$$R_2 = R_2(h, R_1; R_0) = \frac{-h^2 - 4(R_0 - R_1)^2}{8(R_0 - R_1)} \quad (6)$$

$$V = \pi \int_0^h f \left(z; h, R_1, \frac{-h^2 - 4(R_0 - R_1)^2}{8(R_0 - R_1)} \right) dz \quad (7)$$

2.2 Delaunay surface model

The toroid approximation in section 2.1 in which the shape of the meniscus is parameterized using (h, R_1, R_2) is physically inaccurate because it does not guarantee that E is stationary at a local minimum over all kinematically admissible variations of f . To ensure that E , or A if we set $F = 0$, is locally minimized, we need to find an h that eventually settles at an h^* that satisfies

$$h^* = \underset{f, h}{\operatorname{argmin}} E(f, h; R_0, V) \quad (8)$$

$$= \underset{f, h}{\operatorname{argmin}} \gamma A(f, h; R_0, V) - Fh \quad (9)$$

$$= \gamma \underset{h}{\operatorname{argmin}} A \left(h; f^*(z; R_0, V, h), R_0, V \right) - Fh \quad (10)$$

with some f^* that minimizes A subject to R_0 and V . That is,

$$A \left(h; f^*(z; R_0, V, h), R_0, V \right) \leq A \left(h; f(z; R_0, V, h), R_0, V \right) \quad \text{for all } f \quad (11)$$

To find the stationary points of f , let Lagrangian $\mathcal{L}(z, f, f')$ be calculated as

$$\mathcal{L}(z, f, f') = f(z) \sqrt{1 + f'(z)^2} - \lambda f^2(z) \quad (12)$$

$$\frac{\partial \mathcal{L}}{\partial f(z)} = \sqrt{1 + f'(z)^2} - 2\lambda f(z) \quad (13)$$

$$\frac{\partial \mathcal{L}}{\partial f'(z)} = \frac{f(z) f'(z)}{\sqrt{1 + f'(z)^2}} \quad (14)$$

The Euler-Lagrange equation gives

$$\frac{d}{dz} \left(\frac{f(z) f'(z)}{\sqrt{1 + f'(z)^2}} \right) = \sqrt{1 + f'(z)^2} - 2\lambda f(z) \quad (15)$$

where the Lagrange multiplier λ , which also embodies the Laplace pressure ΔP and relates to the mean curvature H by the Young-Laplace Equation, is required to maintain the volume constraint. When $\lambda = 0$, Eq. (15) reduces to a minimal surface $f(z) = a \cosh((z+b)/a)$, also known as the catenoid.

Solving Eq. (15) we have the following ODE

$$f''(z) = \frac{(1 + f'(z)^2) (1 - 2\lambda f(z) \sqrt{1 + f'(z)^2})}{f(z)} \quad (16)$$

which can be numerically solved with boundary conditions

$$f \left(\frac{h}{2} \right) = R_1 \quad \text{and} \quad f' \left(\frac{h}{2} \right) = 0 \quad (17)$$

Note that the Lagrange multiplier λ in Eq. (16) has the exact same physical meaning as the mean curvature H in the Young-Laplace equation. It should be constant across the surface.

One way to search for the solution to the ODE in Eq. (16), which represents the exact shape of a liquid bridge with prescribed (h, R_0, V) , is to find the intersection of curves $H(R_1)$ and $V(R_1)$ (Fig. 3(A-B)). A solution does not exist when the two

curves have no intersection, which implies the volume V cannot be satisfied. Otherwise, exactly one point on the $H(R_1)$ curve will correspond to volume V and give the exact shape profile $f''(z)$.

2.3 Comparison of surface free energy

To verify that predictions of the shape of a liquid bridge using the simplified toroidal model is comparable to other models, Fig. 3(C) shows the potential energy $E = \gamma A - Fh$ as a function of h using toroidal approximation, Surface Evolver³¹, and exact Delaunay solution. The Surface Evolver was used to approximate the surface energy when minimized with respect to h for prescribed values of R_0 and V . In addition to the presumed gravity-free configuration, a simulation that included gravity was also performed with Surface Evolver. Since only the equilibrium length h^* , at which E is minimized, will be used for further analysis, the results show a reasonable agreement for h^* among all models. Hence the following analysis will be based on the gravity-free toroidal model.

An energy instability may occur if the liquid bridge is stretched beyond a length $h > h^*$ where $E(h)$ is locally maximized. To minimize E , h will keep increasing and the neck radius R_1 will decrease. Eventually the liquid bridge will rupture when R_1 becomes zero. With the toroidal model, we define the *breaking length* h_{\max} as the value of h at which $E(h)$ is locally maximized.

2.4 Force-length relationship and operation region

To predict the force-length relationship for any given (R_0, V, γ) , the equilibrium length h^* needs to be calculated for all forces $0 \leq F \leq F_{\max}$, where F_{\max} is the bridge-breaking force for which $h = h_{\max}$. Fig. 3(D) shows an example of $F(h^*)$ relationship with $R_0 = 1$ mm, $V = R_0^3$, and $F = 0$, with γ varies between oxidized state (γ_{\min}) and reduced state (γ_{\max}).

We theorize that the operation region of the liquid metal actuator is the area enclosed by the two boundary $F(h^*)$ curves and the curve with all breaking points $h^* = h_{\max}$ with various surface tension γ . Within this region, we can predict the shape, particularly the actuator length h^* , for any prescribed R_0 , V , γ , and F .

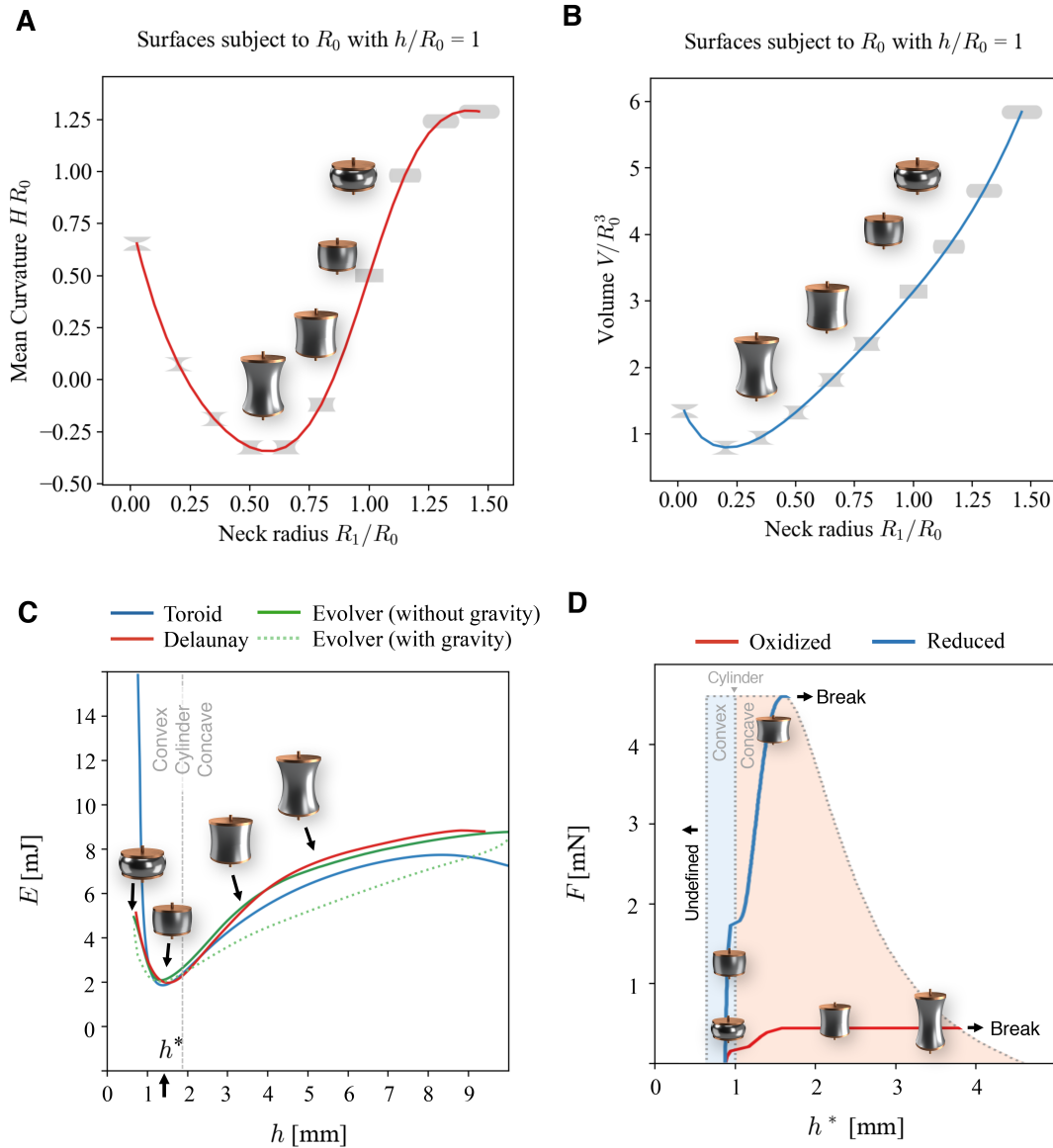


Fig. 3 Theoretical modeling the geometrical and mechanical behavior of LM actuators. (A) Modeled as an exact Delaunay constant-mean-curvature (CMC) surface, the shape of a fixed-volume liquid bridge can be uniquely determined by a characteristic radius R_0 , a neck radius R_1 , and a mean curvature H . (B) Volume of a fixed-mean-curvature liquid bridge at various neck radius R_1 . (A) and (B) collectively enumerate all possible bridge shapes with a certain length h . (C) Surface potential $E = \gamma A - Fh$ as a function of h using three models with $R_0 = 1$ mm and $V = R_0^3$. The liquid bridge tends to assume a length h^* that minimizes E , which shows reasonable agreement among predictions by the toroidal approximation, Surface Evolver³¹, and exact Delaunay solution. In order to verify that gravity can be ignored without significantly changing h^* , simulations in Surface Evolver were performed with (green dotted line) and without gravity (green solid line). (D) Force-length relationship and operation region of EGaln bridge ($\gamma = 50$ mN/m when oxidized and 500 mN/m when reduced) between the fully oxidized state and fully reduced state using the toroidal model with $R_0 = 1$ mm, $V = R_0^3$. The liquid bridge is shown to operate between convex (blue shade) and concave (red shade) regions. Due to the inherent constraint of toroid where $h \geq h_{\min} = 2(R_1 - R_0)$, the shape is undefined for $h^* < h_{\min}$. The breaking length h_{\max} is estimated by finding the local maximum on the toroidal energy in (C), where stretching the liquid bridge beyond h_{\max} will increase h , while decreasing neck radius R_1 , and eventually rupture the liquid bridge.

3 Experimental

In order to characterize the actuation performance and validate the theoretical models, the liquid metal actuator was constructed and tested in response to a given electrical stimulus. The actuator was loaded with its own weight. The motion of the actuator was captured by video for the subsequent shape tracking.

3.1 Fabrication of liquid metal actuators

The liquid metal actuator was constructed by wetting EGaIn (75% gallium and 25% indium mixed by weight, both purchased from RotoMetals) on to the gap between two circular copper plates (both with radius R_0), which were cut from a copper film (thickness 0.1016 mm, purchased from McMaster-Carr) with a UV laser (ProtoLaser U3, LPKF). The laser was configured with a patterning frequency of 50 kHz, power of 3W, and beam diameter of 20 μm . In order to hang the actuator in a balanced manner, two additional strips (width 750 μm) were cut along with the circular plates. To enhance the wettability, the copper plates were submerged in a 1M HCl solution for 10 minutes in order to minimize the presence of copper oxides. Then the complete liquid metal actuator was submerged in a 2M KOH solution.

3.2 Experiment protocol and data analysis

The actuator was loaded by its own weight ~ 2 mN (EGaIn + copper). An electrical pulses ± 2.5 V at 1 Hz was applied between the top copper plate and the surrounding KOH solution. Video of actuation were recorded (Supplementary Video) with a USB microscope camera (Opti-Tekscope OT-HD) in order to measure the actuator length. The video was recorded at 24 frames per second. Customized software was developed to track the top and the bottom points of the liquid bridge in each frame using known dimensions R_0 to infer the actual length.

4 Results and Discussion

The experimental voltage response of a liquid metal actuator with $R_0 = 1\text{mm}$ and $V = R_0^3$ under 1 Hz cyclic activation is shown in Fig. 4. The peak current draw of the actuator was ~ 3.6 mA.

Static and dynamic performance was evaluated from the cyclic test in Fig. 4 without further quasistatic test. One rationale is that the threshold voltage to trigger the redox reactions is independent of the rate of voltage change, and as a result, the actuator will not contract slower at lower actuation frequency. Furthermore, the effect of dynamic loading is orders of magnitude smaller than that of surface tension and therefore is negligible in our analysis.

4.1 Static performance

To benchmark the performance of the liquid metal actuator, common metrics can be calculated from the theoretical model and the experimental data. The most useful static metrics include the strain output, stress output, and work density, which can be evaluated by a hypothetical loading cycle shown in Fig. 5.

In an idealized loading cycle with full range of force and motion, the liquid metal actuator will be stretched isotonically from h_{\min}^* to h_{\max}^* then isometrically from F_{\min} to F_{\max} before return-

ing to the original state. The enclosed area in the $F(h^*)$ plot represents the accumulated net work output, with which the work density can be calculated by

$$\text{Work Density} = \frac{\int_{s \in C} F(s) h^*(s) ds}{\pi \int_0^h f^2 dz} \quad (18)$$

The theoretical calculation of the work density at various scales R_0 (Fig. 5) shows that, in general, the work density of the liquid metal actuator increases logarithmically as R_0 decreases. While decreasing the volume V of the liquid metal can boost the work density at smaller V , it will always hit a plateau where the work density converges to a theoretical limit. The experiment result with a liquid metal actuator with $R_0 = 1\text{mm}$ shows a work density of 2.1 kJ/m³, which is consistent with the theoretical calculation in Fig.5.

Similarly, the theoretical strain and stress output are calculated by considering the ideal loading cycle where the range of motion $h_{\max}^* - h_{\min}^*$ and range of force $F_{\max} - F_{\min}$ are calculated and normalized by the characteristic radius R_0 as

$$\text{Strain} = \frac{h_{\max}^* - h_{\min}^*}{R_0} \quad (19)$$

$$\text{Stress} = \frac{F_{\max} - F_{\min}}{R_0} \quad (20)$$

where the actual cross-sectional area of the actuator varies between R_0 and R_1 axially. The experiment result with a liquid metal actuator with $R_0 = 1\text{mm}$ shows an axial strain $\sim 31.5\%$, again in good agreement with the theory (Fig. 4(E-F)).

4.2 Dynamic performance

In order to estimate the dynamic performance, the liquid metal actuator is simplified using a typical undamped spring model where stiffness $k = dF/dh^*$ arises from the liquid bridge resisting the deformation induced by the change in surface tension γ . Influence by other properties such as the viscosities of the liquid bridge and surrounding electrolyte and electrical potential V are ignored in this work; otherwise a viscoelastic system should be considered³². At $R_0 = 1\text{mm}$ and $V = V_0 = 4\pi R_0^3/3$, a liquid bridge of EGaIn (density $\rho = 6,250$ kg/m³) has a theoretical stiffness $k = 1.9$ N/m and a natural frequency of $\omega = \sqrt{k/m} \approx 72.52$ Hz.

The experiment with a liquid metal actuator with $R_0 = 1\text{mm}$ showed that the actuator is capable of driving at a frequency of at least 1 Hz. Realistically, the operation frequency of the liquid metal actuator will also be influenced by the liquid properties of liquid bridge and surrounding medium. The rate at which the electrochemical oxidation and reduction occurs, which is scale-invariant and related to the activation waveform $V(t)$, will also affect the dynamic of the liquid metal actuator.

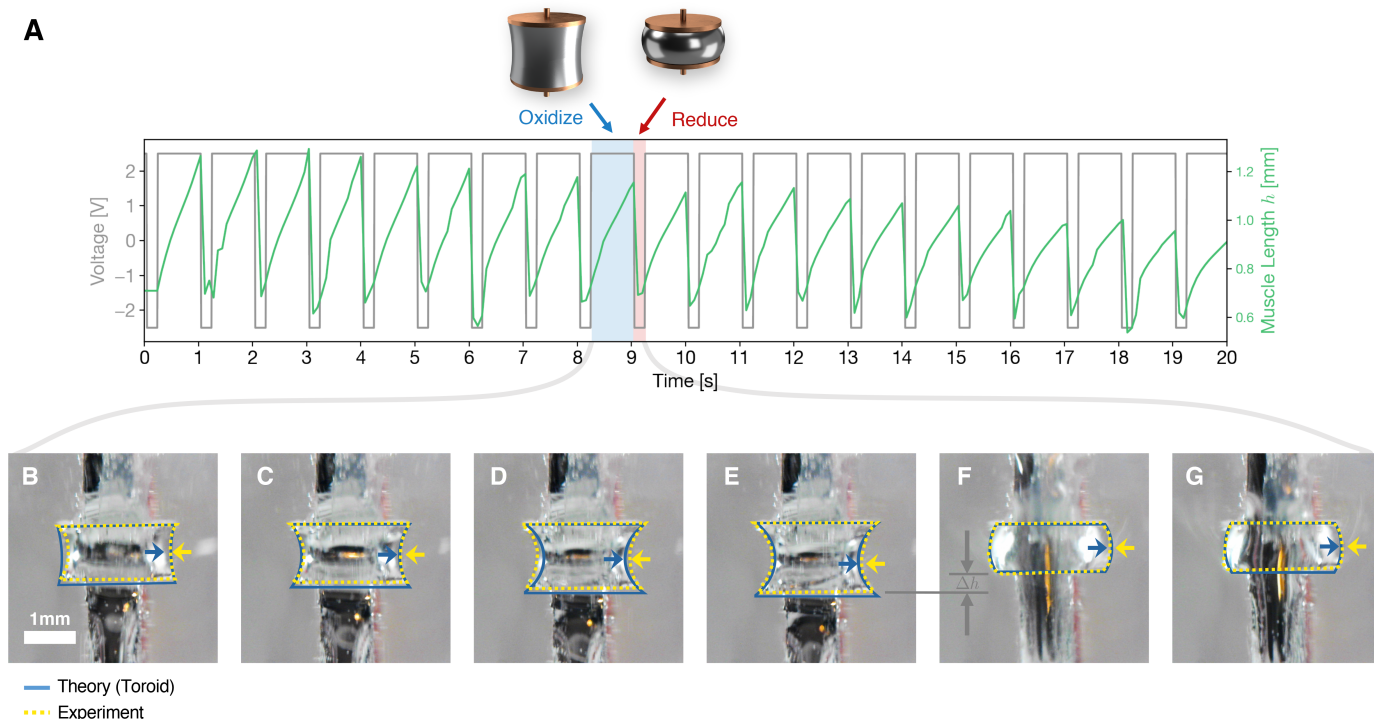


Fig. 4 Video analysis of the liquid metal actuator under periodic 1 Hz activation between oxidized state (blue shade) and reduced state (red state). The actuator is constructed with $R_0 = 1$ mm and $V = R_0^3$ and submerged in a 2M KOH solution. The actuator is loaded by its self weight ~ 2 mN (i.e., the weight of EGaln and copper combined). The actuator extends when the voltage increases and triggers oxidation of gallium. Reduction of gallium oxide causes contraction by restoring the EGaln droplet back to an oxide-free state with high surface energy. (A) Actuator length h during the first 20 cycles. (B-G) Comparison of the experimental shape of the liquid bridge with the toroidal model prediction.

4.3 Byproduct and cycle life

The performance can be degraded by the rapid buildup of byproduct (e.g., H_2 bubbling) during actuation (Fig. 4). Further study is needed to understand the influence of the electrochemical byproduct on the operation and performance of the liquid metal actuator.

4.4 Comparison with existing artificial muscles

The theoretical static and dynamic performance of the liquid metal actuator is compared with natural muscles and a selection of current artificial muscles in Table 1^{6,33–44}. By comparison, the liquid metal actuator has a relatively low operation voltage (~ 1 V) due to the electrochemical properties of gallium, which allows for simpler power consideration in robotic applications.

Another promising feature of the electrochemical LM actuator is the ability to boost the work density by at least one order of magnitude when reducing R_0 , as shown in Fig 5C. This is due to the role of surface tension in dominating force output. For instance, with $V = 0.2R_0^3$, the theoretical work density of the LM actuator will exceed 10^3 kJ/m³ for $R_0 < 2$ μ m, which surpasses dielectric elastomer and shape memory actuators.

In analogy to biological muscles, which is stacked by an ensemble of micron-sized contractile units, the energy density of the liquid metal actuator can be further scaled up by bundling together smaller units. These advantages open the door to new prospects for power-limited systems that require soft actuators with high

work density and low-voltage operation.

4.5 Electrolyte selection

The liquid metal actuator requires an electrolyte surrounding the liquid metal surface to provide continuous flow of ions. In this work, the KOH-water solution was selected due to its high ionic conductivity. However, as a strong base that is highly caustic, KOH can limit the robotic applications of the actuator because of long-term corrosion of the copper plates. Other types of electrolytes are also effective for redox reactions of liquid metals and can be considered in future development. Another drawback is the creation of H_2 gas during water electrolysis at 1.23 V and above. This complicates the packaging of the actuator due to build-up of the gas byproduct. Analogous to waste management in natural muscle tissue, a mechanism will be required to manage byproducts of the electrochemical reaction.

5 Conclusions and outlook

We introduce an artificial muscle unit that is composed of an axis-symmetric capillary bridge of EGaln, which linearly contracts or expands in response to electrical stimuli. The change in electric potential causes a redox reaction that leads to the deposition or removal of gallium oxide and hence the change in surface energy, a phenomenon that goes beyond classical electrocapillarity^{11,45,46}.

We theorized the force-length relationship for a liquid metal

Table 1 Comparison of experimental measurement of the liquid metal actuator ($R_0 = 1$ mm) with selected artificial muscles^{6,33–44}.

Property	Liquid Metal Actuator ($R_0 = 2$ mm)	Muscle	DEA	SMA	LCE
Strain (%)	~ 26	20	$\sim 10^3$	~ 10	30
Stress (MPa)	~ 0.5	0.1	~ 10	$\sim 10^3$	0.25
Work Density (kJ/m^3)	$\sim 10^2$	8	$\sim 10^2$	$\sim 10^3$	~ 10
Frequency (Hz)	~ 10	20	$\sim 10^4$	~ 10	100
Operation Voltage (V)	~ 1	0.1	$\sim 10^3$	~ 10	$\sim 10^3$

actuator unit by modeling the equilibrium shape at any given loading condition. The models are used to predict the static and dynamic performance of the actuator at varying length scale R_0 and volume V . The numerical results inform the design rules to optimize a specific performance of the liquid metal actuator.

The integration of this actuator into soft machines, microfluidic systems, and robotic applications will be governed by the following factors. First, the electrochemical implementation, such as the selection of electrolyte to prevent or suppress gas formation, will have the biggest impact on the artificial muscle package. Second, the axial symmetry of the LM actuator will influence the actual strain and stress output. Third, breaking of the EGaIn bridge needs to be prevented by the incorporation of mechanical stops. The unique combination of low operating voltage, high work density, and decent frequency for the LM actuator show promises for future soft robotic systems.

6 Acknowledgements

The authors acknowledge support from the National Oceanographic Partnership Program (NOPP) under Grant No. N000141812843 (PM: Dr. Reginald Beach) and the Office of Naval Research under Grant No. N00014-18-1-2775 (PM: Dr. Thomas McKenna).

References

- L. Hines, K. Petersen, G. Z. Lum and M. Sitti, *Advanced materials*, 2017, **29**, 1603483.
- S. Kim, C. Laschi and B. Trimmer, *Trends in biotechnology*, 2013, **31**, 287–294.
- F. Ilievski, A. D. Mazzeo, R. F. Shepherd, X. Chen and G. M. Whitesides, *Angewandte Chemie*, 2011, **123**, 1930–1935.
- W. Hu, G. Z. Lum, M. Mastrangeli and M. Sitti, *Nature*, 2018, **554**, 81–85.
- F. Carpi, D. De Rossi, R. Kornbluh, R. E. Pelrine and P. Sommer-Larsen, *Dielectric elastomers as electromechanical transducers: Fundamentals, materials, devices, models and applications of an emerging electroactive polymer technology*, Elsevier, 2011.
- T. Mirfakhrai, J. D. Madden and R. H. Baughman, *Materials today*, 2007, **10**, 30–38.
- S. Seok, C. D. Onal, K.-J. Cho, R. J. Wood, D. Rus and S. Kim, *IEEE/ASME Transactions on mechatronics*, 2012, **18**, 1485–1497.
- M. R. Khan, C. B. Eaker, E. F. Bowden and M. D. Dickey, *Proceedings of the National Academy of Sciences*, 2014, **111**, 14047–14051.
- M. D. Dickey, R. C. Chiechi, R. J. Larsen, E. A. Weiss, D. A. Weitz and G. M. Whitesides, *Advanced functional materials*, 2008, **18**, 1097–1104.
- Y. Lin, J. Genzer and M. D. Dickey, *Advanced Science*, 2020, 2000192.
- C. B. Eaker and M. D. Dickey, *Applied Physics Reviews*, 2016, **3**, 031103.
- C. B. Eaker, D. C. Hight, J. D. O'Regan, M. D. Dickey and K. E. Daniels, *Physical Review Letters*, 2017, **119**, 174502.
- S.-Y. Tang, V. Sivan, P. Petersen, W. Zhang, P. D. Morrison, K. Kalantar-zadeh, A. Mitchell and K. Khoshmanesh, *Advanced Functional Materials*, 2014, **24**, 5851–5858.
- J. Wissman, M. D. Dickey and C. Majidi, *Advanced Science*, 2017, **4**, 1700169.
- L. Hu, L. Wang, Y. Ding, S. Zhan and J. Liu, *Advanced Materials*, 2016, **28**, 9210–9217.
- J. Wu, S.-Y. Tang, T. Fang, W. Li, X. Li and S. Zhang, *Advanced materials*, 2018, **30**, 1805039.
- S. Xu, B. Yuan, Y. Hou, T. Liu, J. Fu and J. Liu, *Journal of Physics D: Applied Physics*, 2019, **52**, 353002.
- A. Zavabeti, T. Daeneke, A. F. Chrimes, A. P. O'Mullane, J. Z. Ou, A. Mitchell, K. Khoshmanesh and K. Kalantar-Zadeh, *Nature communications*, 2016, **7**, 1–10.
- F. Li, S. Kuang, X. Li, J. Shu, W. Li, S.-Y. Tang and S. Zhang, *Advanced Materials Technologies*, 2019, **4**, 1800694.
- M. R. Khan, C. Trlica and M. D. Dickey, *Advanced Functional Materials*, 2015, **25**, 654–654.
- L. Russell, J. Wissman and C. Majidi, *Applied Physics Letters*, 2017, **111**, 254101.
- J. Zhang, Y. Yao, L. Sheng and J. Liu, *Advanced Materials*, 2015, **27**, 2648–2655.
- X. Li, J. Xie, S.-Y. Tang, R. Xu, X. Li, W. Li and S. Zhang, *IEEE Transactions on Industrial Informatics*, 2018, **15**, 2535–2543.
- R. C. Gough, J. H. Dang, M. R. Moorefield, G. B. Zhang, L. H. Hihara, W. A. Shiroma and A. T. Ohta, *ACS applied materials & interfaces*, 2016, **8**, 6–10.
- G. Li, J. Du, A. Zhang and D.-w. Lee, *Journal of Applied Physics*, 2019, **126**, 084505.
- K. B. Ozutemiz, J. Wissman, O. B. Ozdoganlar and C. Majidi, *Advanced Materials Interfaces*, 2018, **5**, 1701596.
- M. Mastrangeli, *Advanced Materials*, 2015, **27**, 4254–4272.
- G. Lian, C. Thornton and M. J. Adams, *Journal of colloid and interface science*, 1993, **161**, 138–147.
- D. Megias-Alguacil and L. J. Gauckler, *Granular Matter*, 2011, **13**, 487–492.
- C. D. Willett, M. J. Adams, S. A. Johnson and J. P. Seville, *Langmuir*, 2000, **16**, 9396–9405.
- K. A. Brakke, *Experimental mathematics*, 1992, **1**, 141–165.
- J.-B. Valsamis, M. Mastrangeli and P. Lambert, *European Journal of Mechanics-B/Fluids*, 2013, **38**, 47–57.
- J. D. Madden, N. A. Vandesteeg, P. A. Anquetil, P. G. Madden, A. Takshi, R. Z. Pytel, S. R. Lafontaine, P. A. Wieringa and

- I. W. Hunter, *IEEE Journal of oceanic engineering*, 2004, **29**, 706–728.
- 34 G. K. Klute, J. M. Czerniecki and B. Hannaford, 1999 IEEE/ASME International Conference on Advanced Intelligent Mechatronics (Cat. No. 99TH8399), 1999, pp. 221–226.
- 35 G. K. Klute, J. M. Czerniecki and B. Hannaford, *The International Journal of Robotics Research*, 2002, **21**, 295–309.
- 36 C. Keplinger, J.-Y. Sun, C. C. Foo, P. Rothemund, G. M. Whitesides and Z. Suo, *Science*, 2013, **341**, 984–987.
- 37 B. K. Juluri, A. S. Kumar, Y. Liu, T. Ye, Y.-W. Yang, A. H. Flood, L. Fang, J. F. Stoddart, P. S. Weiss and T. J. Huang, *Acs Nano*, 2009, **3**, 291–300.
- 38 I. W. Hunter and S. Lafontaine, Technical Digest IEEE solid-state sensor and actuator workshop, 1992, pp. 178–185.
- 39 C. S. Haines, M. D. Lima, N. Li, G. M. Spinks, J. Foroughi, J. D. Madden, S. H. Kim, S. Fang, M. J. De Andrade, F. Göktepe *et al.*, *science*, 2014, **343**, 868–872.
- 40 M. Bozlar, C. Punckt, S. Korkut, J. Zhu, C. Chiang Foo, Z. Suo and I. A. Aksay, *Applied Physics Letters*, 2012, **101**, 091907.
- 41 Q. Zhao, J. W. Dunlop, X. Qiu, F. Huang, Z. Zhang, J. Heyda, J. Dzubiella, M. Antonietti and J. Yuan, *Nature communications*, 2014, **5**, 1–8.
- 42 H. Yuk, S. Lin, C. Ma, M. Takaffoli, N. X. Fang and X. Zhao, *Nature communications*, 2017, **8**, 1–12.
- 43 E. Palleau, D. Morales, M. D. Dickey and O. D. Velev, *Nature communications*, 2013, **4**, 1–7.
- 44 J. Huber, N. Fleck and M. Ashby, *Proceedings of the Royal Society of London. Series A: Mathematical, physical and engineering sciences*, 1997, **453**, 2185–2205.
- 45 D. C. Grahame, *Chemical reviews*, 1947, **41**, 441–501.
- 46 A. Frumkin, N. Polianovskaya, N. Grigoryev and I. Bagot-skaya, *Electrochimica Acta*, 1965, **10**, 793–802.

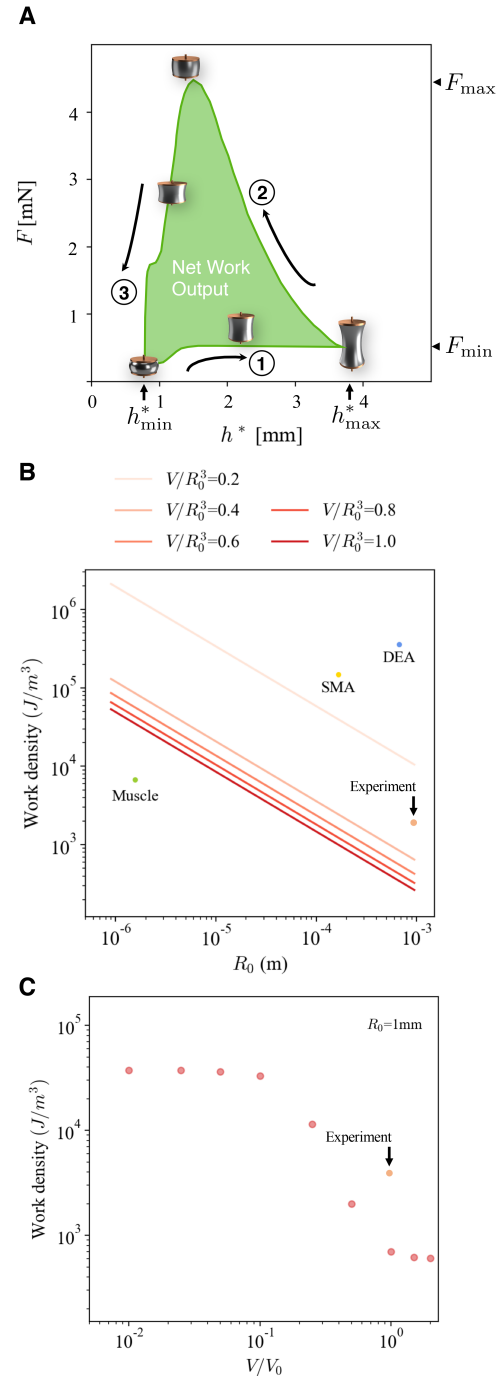


Fig. 5 Evaluation of work density of LM actuator. (A) Hypothetical loading cycle. Using toroidal approximation, the actuator is loaded around the boundaries of the $F - h^*$ curves. (1) At fully oxidized state, the actuator undergoes axial expansion from h^*_{min} to h^*_{max} , the theoretical maximum length, while being prevented from breaking. The actuator ends up loading F_{min} at the theoretical maximum length h^*_{max} . (2) The actuator goes from oxidized state to reduced state without breaking and arrives at F_{max} , the theoretical maximum force of the actuator. (3) Decreasing load from F_{max} to F_{min} restores the actuator back to the natural state. (B) Theoretical work density of LM actuator at various scales R_0 . Comparison is made with natural muscle, dielectric elastomer, and shape memory alloy. (C) When fixing at a scale R_0 , the theoretical work density of LM actuator at various volumes V .